AGU PUBLICATIONS

JGR

Journal of Geophysical Research: Atmospheres

RESEARCH ARTICLE

10.1002/2014JD022296

Key Points:
- Analysis of the imbalance of the observed surface energy budget
- Daily and nightly averaged annual cycles of the observed SEB
- Comparison between ECMWF model values and observations

Correspondence to:
J. Cuxart,
joan.cuxart@uib.cat

Citation:
Cuxart, J., L. Conangla, and M. A. Jiménez (2015), Evaluation of the surface energy budget equation with experimental data and the ECMWF model in the Ebro Valley, *J. Geophys. Res. Atmos.*, *120*, 1008–1022, doi:10.1002/2014JD022296.

Received 10 JUL 2014
Accepted 27 DEC 2014
Accepted article online 6 JAN 2015
Published online 12 FEB 2015

Evaluation of the surface energy budget equation with experimental data and the ECMWF model in the Ebro Valley

J. Cuxart[1], L. Conangla[2], and M. A. Jiménez[3]

[1]Department of Physics, University of the Balearic Islands, Palma de Mallorca, Spain, [2]Department of Applied Physics, Polytechnic University of Catalonia, Manresa, Spain, [3]Department of Global Change Research, Mediterranean Institute for Advanced Studies (UIB-CSIC), Esporles, Spain

Abstract In numerical models of the climate system and in other applications, the surface energy budget is usually considered closed, allowing for estimation of missing terms as the residual of the others. Real measurements of this budget show significant uncertainties in the values of each flux and imbalances that range between 5% and more than 50%, as shown in recent literature. In this article, a derivation of the surface energy budget equation from the prognostic temperature equation is presented and the hypotheses are discussed. Minor terms, which are usually neglected, such as tendency or advection, are estimated. Then, the 2 year statistics for a station in the Ebro Valley are analyzed, focusing on the imbalance, which is found to increase as the other terms in the equation increase, with values on the order of 30% of the net radiation. The same location seen by the model of the European Center for Medium-Range Weather Forecasts (ECMWF) is analyzed. Large differences between observations and model simulation results occur at a daily scale although the average terms are comparable, with a systematic overestimation of the ground and sensible heat fluxes by the model.

1. Introduction

The surface energy budget (SEB) is a balance equation for a surface or volume, typically applied to the interface between the atmosphere and the elements of the surface. It accounts for inputs, outputs, and storage in the internal constituents. Traditionally, the budget is taken for an infinitesimal volume comprising the interface for steady state conditions, with no storage or tendency. This classical formulation is

$$Rn + H + LE + G = 0 \tag{1}$$

where the net radiation (Rn) is the main input (or output) of energy during daytime (nighttime) and drives the sensible (H) and latent (LE) turbulent heat fluxes and the ground heat flux (G). An extensive discussion on the equation may be found in reference books such as the classical textbook of *Garratt* [1992].

This equation is used in a number of applications, both for measurement and modeling aspects, often obtaining one of the terms (usually LE or G) as the residual of the others, for which there are measurements or estimations. Examples can be found for remote sensing [*Bastiaanssen et al.*, 1998], agricultural applications [*Sánchez et al.*, 2008], and numerical modeling [*Viterbo and Beljaars*, 1995].

Despite the widely used simplified form of equation (1), more processes modify the energy of the volume for which the SEB is applied and are customarily neglected. These include advection of heat due to local heterogeneities, as well as transient conditions such as morning or evening transitions or cloud passages, as equation (1) implicitly assumes homogeneous terrain and steady state conditions during the computation period. Storage in the elements of the volume and biological processes involving energy exchanges or unaccounted water phase changes are also usually ignored. The current knowledge on the importance of these processes can be found, among others, in *Mauder et al.* [2007], *Oncley et al.* [2007], *Foken* [2008], *Moderow et al.* [2009], and *Leuning et al.* [2012].

Even under homogeneous and steady state conditions, there are fundamental issues remaining. The form of equation (1) implies a box of differential volume for which the four different terms can be determined. However, sensors are installed at different locations and heights and report different physical influences, as described in *Foken* [2008]. Each sensor has its own error range and the total error can be large when

one of the terms is estimated as the residual of the equation [*Oncley et al.*, 2007]. The different time scales contributing to each term have been analyzed [e.g., *Oncley et al.*, 2007 or *Foken*, 2008], and this issue is minimized only if the averaging times are large enough to include them. This implies that the available imbalances computed using 30 min averages include effects of longer time scale processes, but *Foken et al.* [2010] considered these effects not to be significant if the average time is increased to 2 h.

In many numerical models, such as that of the European Center of Medium-Range Weather Forecasts (ECMWF) [*Viterbo and Beljaars*, 1995], computed values of Rn, H, and LE, assuming that the residual is G, are used to determine the surface temperature equation with an iterative approach. The different fluxes are expressed as functions of some parameters that may be adjusted and have to be continuously checked against observations. In some configurations, such as in the case of clear nights with weak winds, the model errors can become large and have led to significant modifications of the schemes (such as in *Viterbo et al.* [1999]).

The main objective of this work is to quantify the imbalance for a particular station, looking for patterns related to the time of the day or the season of the year, and to see how a numerical model compares with the available observations. In the following section, we relate the SEB to the prognostic temperature equation to provide a formal framework for our analysis. In section 3, we proceed to compute the imbalance for 2 years of observations in the Raimat station belonging to the Meteorological Service of Catalonia in the eastern Ebro Valley, in the Iberian Peninsula. Relations between the computed imbalance and the rest of the terms of the SEB and some meteorological variables are inspected to see which conditions maximize the imbalance during the day and night in the different seasons of the year. A term-by-term comparison to the ECMWF corresponding model values, in which the SEB is closed, is made in section 4 to determine differences and highlight possible consequences in the model runs. Some conclusions are provided in section 5.

2. A Framework for the Surface Energy Budget Equation

2.1. The Prognostic Temperature Equation for a Volume Across the Interface

The prognostic temperature equation is used here as a framework to discuss the different terms measured and those usually neglected that contribute to the imbalance of the SEB. Temperature is used instead of potential temperature because these differences are minor close to the surface. In addition, this approach allows to locate each term of the budget at the position where it is actually measured or computed in the volume. This equation can be expressed as

$$\frac{\partial \overline{T}}{\partial t} + \overline{u_i}\frac{\partial \overline{T}}{\partial x_i} = -\frac{1}{\rho C_p}\frac{\partial \overline{Rn}}{\partial x_i} - \frac{\partial \overline{u_i' T'}}{\partial x_i} - \frac{\partial \overline{G^*}}{\partial x_i} + \overline{S^*} + \overline{B^*} + \overline{LE^*} + Ot^* \tag{2}$$

where the Einstein summation convention is used. The overline indicates an average value for the computation period and the accent shows a deviation from this average. The left-hand side is equivalent to the total derivative of T, expanded as the sum of the Temperature Tendency (TT^*), and the advection term (A^*). On the right-hand side, there are the divergences of the net radiation (Rn), turbulent fluxes that arise from the Reynolds decomposition ($\overline{u_i' T'}$) and the molecular heat flux (G^*). They are followed by some source terms distributed in the volume, namely the storage in the mass elements (S^*), the biological processes (B^*), the phase changes of water (LE^*), and other processes or factors, which also may include instrumental errors (Ot^*). C_p and ρ are the specific heat and the density of the air, which are the parameters used to convert W m^{-2} to K s^{-1}.

The molecular heat flux is customarily neglected in the air but it is very important in the soil. Furthermore, the storage of energy in the soil is included here in G, following the standard calorimetric approach proposed by the manufacturer of the heat plate using values of temperature and soil moisture of the layer between the surface and the plate, a procedure that allows G to be considered as if it were located very close to the surface.

For the purposes of our discussion, we will drop the overlines for the average values—except for the turbulent fluxes—and restrict our equation to a 2-D framework. Furthermore, here we will only consider the vertical divergences, implying that smaller-scale motions than the resolved horizontal advection remain in the term Ot^*. A negative divergence of any flux will result in heating the volume considered. Finally,

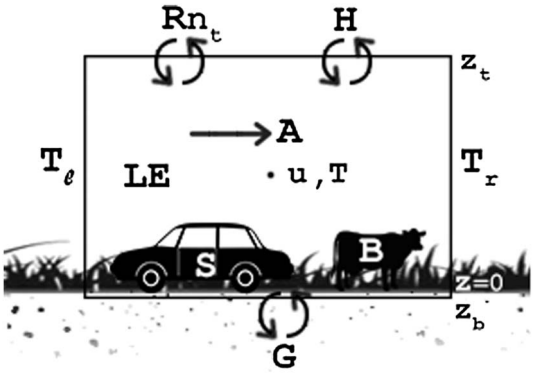

Figure 1. A conceptual diagram of the surface energy balance, with a lower boundary condition into the soil and an upper boundary condition in the atmosphere. *Rn* stands for the net radiation, *H* for the turbulent sensible heat flux, *LE* for the heat related to phase changes, *G* for the ground heat flux, *S* for the storage, *B* for the biological processes, *A* for the advection across the box between temperature T_l and T_r. *T* and *u* stand for the temperature and the wind speed, and z_t and z_b for the height of the top and bottom of the box.

let us assume that *u* is the predominant wind direction (positive pointing to the right) and that the average vertical wind speed is zero, leading to

$$\frac{\partial T}{\partial t} + u\frac{\partial T}{\partial x} = -\frac{1}{\rho C_p}\frac{\partial Rn}{\partial z} - \frac{\partial \overline{w'T'}}{\partial z} - \frac{\partial G^*}{\partial z} + S^* + B^* + LE^* + Ot^* \quad (3)$$

We conceptually apply this equation to the usual experimental configuration, which uses measurements from a few meters above the surface and a few centimeters below the ground. The equation can also be used for the usual model approach, which computes values at the first flux and mass model levels in the air and at a layer adjacent to the surface for the soil values (Figure 1). We can consider this the prognostic equation of the temperature of the volume, with the advection term only applicable to the air part between the left and right arbitrary limits (marked *l* and *r*, respectively). Let us also assume that the sources (phase changes included) can be anywhere in the volume and that the heat fluxes are at the top and bottom limits of the box (marked *t* and *b*, respectively).

$$\frac{\Delta T}{\Delta t} + u\frac{(T_r - T_l)}{x_r - x_l} = -\frac{1}{\rho C_p}\left(\frac{Rn_t - Rn_b}{z_t - z_b}\right) - \left(\frac{\overline{w'T'}_t - \overline{w'T'}_b}{z_t - z_b}\right) - \left(\frac{G_t^* - G_b^*}{z_t - z_b}\right) + S^* + B^* + LE^* + Ot^* = 0 \quad (4)$$

To reach the final form of this conceptual equation, we assume that radiation and turbulence in the soil are zero, the molecular conductivity of heat in the air can be neglected, and we mark the turbulence flux at the top as H^*. For the sake of simplicity we approximate $(z_t - z_b)$ to z_t because z_b is usually much smaller than z_t in absolute value and multiply the equation by $z_t \rho C_p$

$$z_t \rho C_p\left(\frac{\Delta T}{\Delta t} + u\frac{(T_r - T_l)}{x_r - x_l}\right) = -Rn_t - \rho C_p H^* + \rho C_p G^* + z_t \rho C_p(S^* + B^* + LE^* + Ot^*) \quad (5)$$

To express the equation in the traditional form, all the terms of the SEB are written in W m^{-2}, as for the storage and advection terms $TT = z_t \rho C_p \frac{\Delta T}{\Delta t}$, $A = z_t \rho C_p u \frac{(T_r - T_l)}{x_r - x_l}$. We adopt the classical notation *Rn* for the radiation of the upper part, and we take $G = -\rho C_p G^*$. The sensible turbulent heat flux is written $H = \rho C_p H^* = \rho C_p \overline{w'T'}_t$, using the fluxes provided by an eddy-correlation system, or a parameterized value from the vertical gradient of temperature. The phase changes in the box are given by $LE = -z_t \rho C_p LE^* = \rho L_v \overline{w'q'}$, where *q* is the specific humidity and L_v is the latent heat of vaporization of water. Taking the rest of the source terms in W m^{-2} as *S*, *B*, *LE*, and *Ot* (dropping the asterisk), we reach the compact equation

$$TT + A = -\mathbf{Rn} - \mathbf{H} - \mathbf{G} + S + B - \mathbf{LE} + Ot \quad (6)$$

The usual form of the SEB (whose terms are in bold in the preceding equation) is obtained assuming that the tendency, the advection, the storage, the biological, and the other processes can be neglected, leading straight to equation (1), $\mathbf{Rn} + \mathbf{H} + \mathbf{LE} + \mathbf{G} = 0$. For example, at noon a positive radiation flux (downward, *Rn* positive) that heats the surface will be compensated by a sensible heat flux directed upward (*H*, negative), evaporation of water (*LE*, negative), and a ground flux directed downward (*G*, negative).

The imbalance, which will usually have the same sign as *Rn*, reads as

$$\mathbf{Rn} + \mathbf{H} + \mathbf{LE} + \mathbf{G} = -TT - A + S + B + Ot = \mathrm{Imb} \quad (7)$$

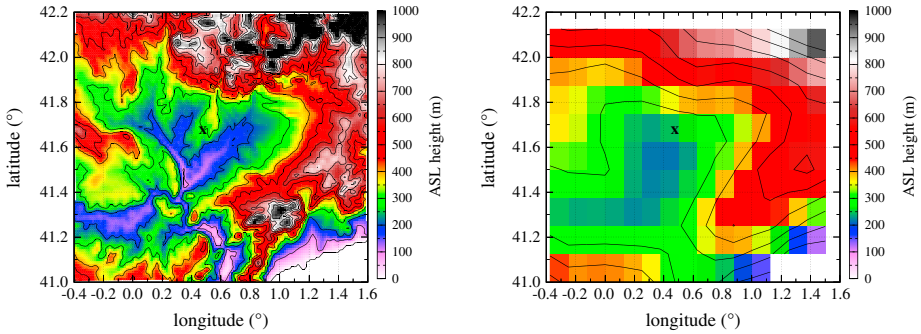

Figure 2. (left) The area surrounding the station at Raimat with a 1 km resolution topography; (right) the topographical representation at the resolution of the ECMWF model (0.125°). The cross represents the location of the Raimat station.

2.2. Scale Analysis of the Imbalance Terms

The main terms of the SEB are well known, and their typical ranges of variation will be illustrated in the next section. Here we provide estimations of the orders of magnitude of the traditionally neglected terms.

Tendency. The tendency may reach its maximum values in the morning transition of a clear day, when an increase of 20 K could take place in 6 h at midlatitudes. The corresponding value would be between 1 and 5 W m^{-2}.

Horizontal Advection. Horizontal advection depends on the scale of the heterogeneities of the surface temperature. For a regional temperature gradient this term is very small. For instance, if the temperature gradient is 1 K/100 km, the horizontal advection is below 0.1 W m^{-2}. Nevertheless, for small-scale heterogeneities this term may become significant. In the case of a temperature gradient of 1 K/100 m, it would be of the order of 50 W m^{-2}.

Storage. If we assume that thermal equilibrium is reached within the computation period between the bodies of the volume and the air (objects, vegetation, etc.), we can estimate the energy used in the process. For instance, if 10 kg of mass per m^3 was considered, as in a dense crop field, using the heat capacity of water and considering 1 K in 1 h, this would provide values of the order of a few W m^{-2}.

Biological processes. Biological processes, such as the plant respiration process may yield, in very dense canopies, less than 10 W m^{-2}, which are used essentially inside the leaf tissue [*Oke*, 1987]. The transpiration that the plants make is more relevant for the SEB, because only a small part of the water moved along the plant is actually used in plant biochemical processes. This may lead to an underestimation of the value of the evapotranspiration.

Others. Any other processes not accounted for by now are impossible to estimate. With respect to instrumental errors, they can include sensor misalignments, missing transport by eddies smaller than the device, or longer time scale processes than the selected averaging period. In some specific locations, vertical advection may be relevant. It can also include energy related to water changes in the surface, the vegetation, and the soil that may not reach the measuring device a few meters above the surface. This term could easily account for several tens of W m^{-2}.

3. Analysis of the Raimat Data

3.1. Location, Instrumentation, and Data

A site in the eastern Ebro Basin was chosen for this study, the station in the Raimat vineyards (41°41′*N*, 0°34′*E*, Figure 2a), in Catalonia. Two complete years (2009 and 2010) of SEB data are available and will be analyzed in this section. The characteristics of the site are described in detail in *Cuxart et al.* [2012]; the site is located in a clearing among vineyards on a flat plateau in the lowermost area of the Ebro Basin, which is a closed, triangular basin, limited by the Pyrenees to the north, the Iberian System to the southwest, and the Catalan precoastal ranges to the east. The climate is semiarid, but the lowlands are extensively irrigated in the summer months.

The two predominant regimes are the synoptic westerlies and the local circulations. *Martínez et al.* [2008] and *Cuxart et al.* [2012] documented the diurnal cycle of the latter. During the day, after the morning transition, winds blow upslope from the wet lowlands to the drier warmer gentle slopes surrounding

Table 1. The 2009 and 2010 Average Observed and Model Values of the Terms of the SEB[a]

			TT	*A*	*Rn*	*H*	*LE*	*G*	Imb
1200–1500 UTC	annual	station	0.47	0.06	365.8	−64.7	−155.9	−36.6	104.0
		model	0.23	−0.03	347.8	−148.6	−140.4	−58.9	0
	winter	station	0.37	0.07	180.1	−50.8	−50.4	−23.2	59.4
		model	0.23	−0.06	186.1	−66.7	−76.9	−42.5	0
	spring	station	0.46	0.03	435.4	−84.8	−185.8	−47.1	116.3
		model	0.23	−0.02	412.1	−180.2	−162.0	−70.0	0
	summer	station	0.62	0.11	555.9	−65.2	−284.5	−57.1	142.5
		model	0.27	−0.02	509.3	−229.0	−204.2	−76.1	0
	fall	station	0.44	0.04	293.3	−56.4	−104.8	−22.7	105.2
		model	0.17	−0.02	279.5	−116.3	−116.8	−46.3	0
0000–0300 UTC	annual	station	−0.29	0.21	−40.2	14.3	−7.5	23.0	−11.7
		model	−0.28	0.00	−56.7	13.7	−2.9	45.9	0
	winter	station	−0.16	0.25	−33.5	11.0	−4.3	19.2	−8.0
		model	−0.16	−0.05	−52.1	17.8	−1.8	36.1	0
	spring	station	−0.33	0.23	−41.8	15.3	−9.2	22.0	−14.6
		model	−0.33	0.01	−57.9	13.3	−3.6	42.8	0
	summer	station	−0.38	0.16	−47.6	21.2	−14.0	27.3	−15.4
		model	−0.37	0.04	−59.5	10.6	−3.5	52.4	0
	fall	station	−0.30	0.22	−38.1	9.9	−2.5	23.3	−8.9
		model	−0.24	−0.02	−57.3	13.2	−2.7	46.9	0

[a]Units: W m^{-2}. The imbalance is the average of individual imbalances.

them, whereas a reverse circulation takes place at night, with well-defined low-level jets from the E and SE, originating from the slopes, which are colder than the plain at night. These circulations are more intense in summer, when the regional thermal gradients are stronger. This regime, as documented in *Martínez et al.* [2008], took place for 37% of the time between 1997 and 2005. In the wintertime, fog is a frequent phenomenon and its characteristics in the area have been described by *Cuxart and Jiménez* [2012].

In Raimat there is an operational, automated weather station belonging to the Meteorological Service of Catalonia that, between December 2008 and February 2011, was supplemented with equipment measuring turbulent heat, momentum, humidity, and CO_2 fluxes (a sonic anemometer Campbell model CSAT-3 and an openpath fast gas analyzer LiCoR model 7500), the four components of the radiation budget (Kipp and Zonen CNR1), ground heat flux (a Hukseflux self-calibrated heat plate), and soil temperature and water content (Campbell CS 616). As mentioned before, the ground flux was corrected for heat storage in the layer above the plate. The analyzed time series consists of half-hourly averages and standard deviations of the different quantities computed, as provided by the Campbell software package, which includes the *Webb et al.* [1980] correction for the latent heat flux. Radiation uncertainties are of the order of 25 W m^{-2} during the daytime and 10 W m^{-2} at night [*Kohsiek et al.*, 2007].

Here we select the daily averaged values for the 3 h intervals 1200–1500 UTC and 0000–0300 UTC because these time intervals are, respectively, daytime and nighttime all year in the location that was analyzed and allow for consistent analyses for the whole 2 year series. Moreover, the values that can be obtained from the model of the European Center of Medium-Range Weather Forecasts (ECMWF) are 3 h averages, making our data-averaged values directly comparable to the model data in section 4.

3.2. Annual Averages and Evolution

The SEB is estimated for the Raimat site using the annual and seasonal averages displayed in Table 1 for the intervals 1200–1500 UTC ("noon") and 0000–0300 UTC ("midnight"), and also looking at the annual cycle using monthly averages (Figure 3) and individual 3 h averages in the *x* axes (Figure 7). Note that the daily extreme values may not occur during these periods.

We see that *TT* is usually below 1 W m^{-2}, positive near noon and negative near midnight. For 10 km scales, *A*, computed with the nearby stations of Alfarràs (18.5 km to the northeast) and Gimenells (5.4 km to the southwest), is also of the order of 1 W m^{-2} . Therefore, these two processes will be neglected from now on, keeping in mind that *A* may be important at smaller scales, an effect that will remain in the imbalance.

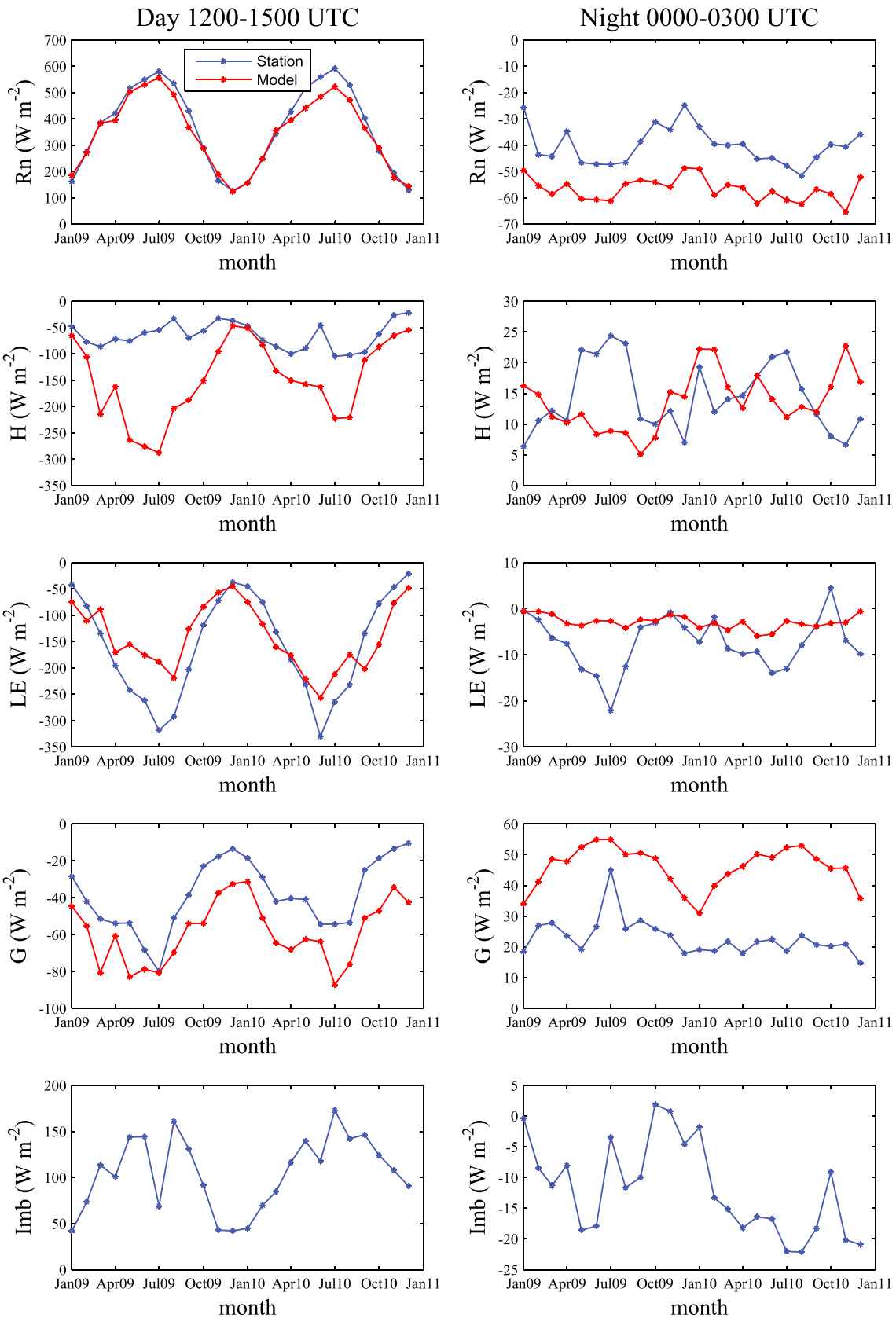

Figure 3. Evolution of the monthly averages of the surface energy budget terms. (left) Average value for 1200–1500 UTC. (right) Average value for 0000–0300 UTC. (top to bottom) Net radiation (*Rn*), sensible heat flux (*H*), latent heat flux (*LE*), ground flux (*G*), and imbalance (Imb) for observed (blue) and ECMWF (red).

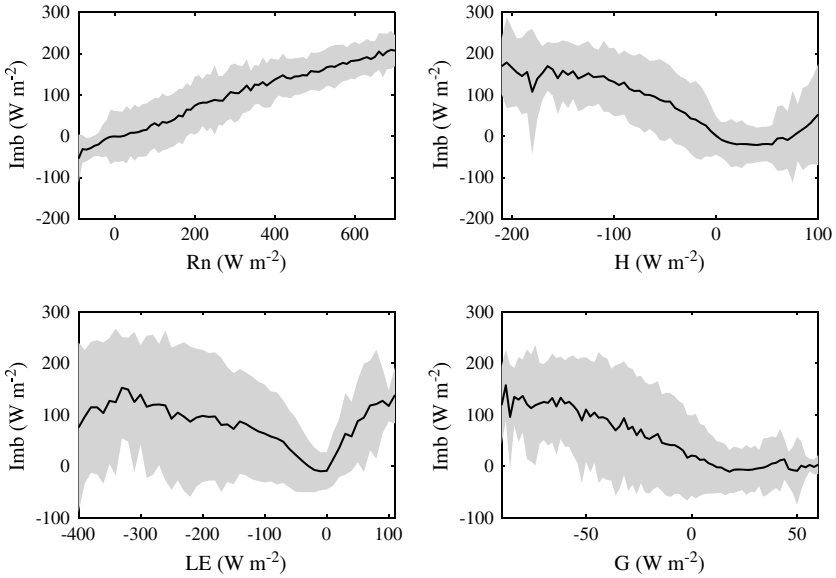

Figure 4. The imbalance as a function of the main terms of the observed SEB (all data). Values are the averages of the imbalances for a particular interval of the SEB term. The black line represents the average values and the shaded grey area the standard deviation.

The net radiation, computed from the balance of the four measured components is, on average, the largest term at noon, with a clear annual cycle, from 180 W m^{-2} in winter to 556 W m^{-2} in summer. The annual cycle is less defined at midnight, with seasonal values varying from −34 W m^{-2} in winter to −48 W m^{-2} in summer.

H and *LE* are commented together. At noon, the annual averages show that *LE* is 2.4 times larger than *H*. Monthly evolutions in Figure 3 indicate that *LE* has a well-defined annual cycle, whereas *H* varies much less and without a clear annual cycle. This is most likely linked to the large availability in the site of soil moisture, due to irrigation in the warm part of the year, implying that most of the radiative energy input is used for evaporation. However, in winter, the two quantities have comparable values, due to the net radiation minimum and the seasonal lack of irrigation. At midnight the situation is completely different. On average *H* is bringing heat to the surface while *LE* removes heat through evaporation. However, the value of *LE* is the result of averaging positive (condensation) and negative (evaporation) values and, for individual 3 h averages, *LE* and *H* can be similar in value (Figure 7). The largest average values of *H* and *LE* are found in summer, when the soil is warmer and the low-level jets are most intense, increasing turbulent mixing, as described in *Cuxart et al.* [2012].

The ground flux (*G*) is the fourth term of importance at noon, showing an annual cycle with a clear maximum in summer. It is approximately 10% of the value of the net radiation. At night, the term becomes the second in magnitude, with absolute values greater than half the net radiation, and no well-defined annual cycle.

The imbalance (Imb) follows a similar pattern as the radiation, an annual cycle at noon peaking in summer and no cycle at midnight. During the daytime the values of the imbalance are approximately 34% *Rn* in fall and winter and 27% in spring and summer, whereas for the nighttime, spring and summer are close to 33% *Rn* and fall and winter approximately 24% *Rn*. These imbalances include subkilometric scale advection—related to surface heterogeneities—heat storage in the mass elements, biological processes that are thermally relevant, and instrumental uncertainties, such as unaccounted latent heat flux in the soil and over vegetation. On average the imbalance has the same sign as *Rn*, meaning that the radiative forcing is not compensated by the main terms of the SEB.

Compared to other recent studies, in the case of sites with a less complex terrain, LITFASS-2003 has imbalances on the order of 20% of the net radiation [*Foken et al.*, 2010], and EBEX (Energy Balance Experiment) is above 10% [*Oncley et al.*, 2007]. Studies carried out over more complex terrain, such as the Loess Plateau in Tibet, have imbalances close to 15% during the day and above 40% at night [*Yue et al.*, 2012].

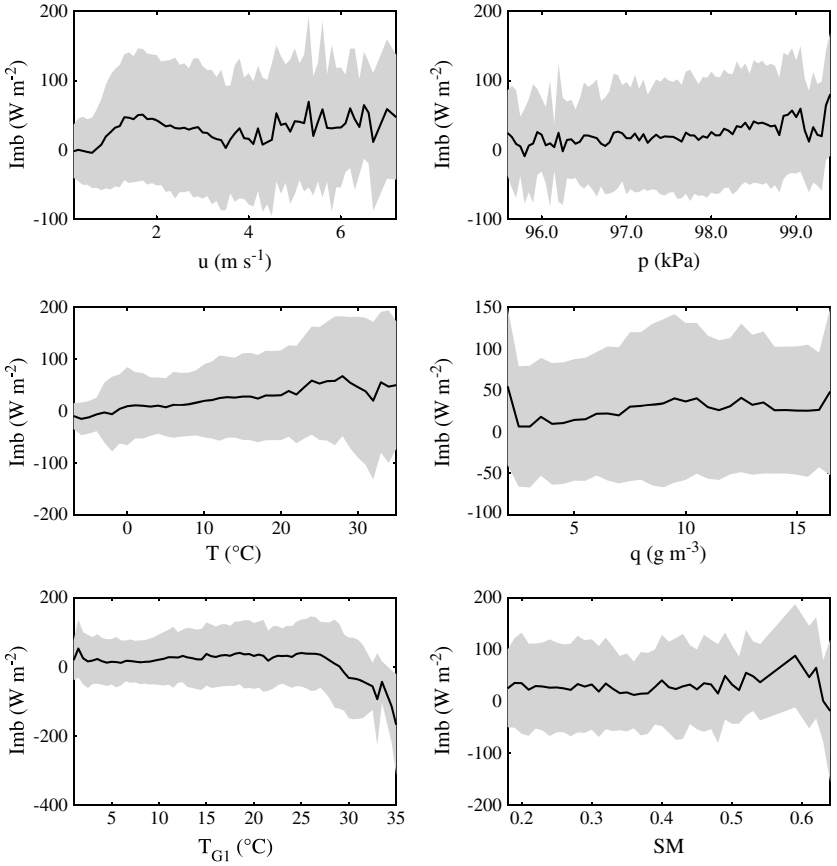

Figure 5. The imbalance as a function of several relevant atmospheric and soil variables (all data). Values are the averages of the imbalances for a particular interval of the variable. (left to right and top to bottom) Wind speed, surface pressure, air temperature, specific humidity, soil temperature (*TG*1), and soil moisture. The black line represents the average values and the shaded grey area the standard deviation.

We can see that our imbalances are relatively large in the daytime, whereas the values at night are between those of flat heterogeneous terrain and those of mountainous terrain.

It is worth noting that for the other times of the day, the annual averages are difficult to interpret, because they include daytime and nighttime values. Nevertheless, the general behavior of the average values (not shown) indicates that the fluxes and the imbalance increase from 0700 UTC until 1200 UTC and decrease afterward until 1600 UTC, whereas at nighttime they have almost constant average values. A special time is 1700 UTC, when *Rn* is still positive but smaller than Imb and *G*, reflecting the evening transition process.

3.3. Imbalance Versus the Other Terms of the Budget

Figure 4 displays the different terms of the observed SEB against the imbalance for all hours (not only for 1200–1500 UTC and 0000–0300 UTC). The values are obtained by averaging imbalance values inside each variable bin, and the mean and the standard deviation are shown.

Table 2. The 2009–2010 Observed Averages for 1200–1500 UTC, Ordered by Imbalance Values[a]

1200–1500 UTC	% of Data	Imb	*Rn*	*H*	*LE*	*G*	*u* (m s^{-1})	*p* (kPa)	*T* (°C)
Imb <60	26	33	157	−36	−64	−23	2.5	97.6	11.7
60 ≤ Imb <100	21	80	298	−68	−117	−33	2.8	97.7	14.8
100 ≤ Imb <150	30	126	436	−79	−186	−45	2.4	98.0	20.5
Imb ≥ 150	23	179	522	−80	−220	−45	2.2	98.0	24.8

[a]Terms of the energy balance in W m^{-2}.

Table 3. The 2009–2010 Observed Averages for 0000–0300 UTC, Ordered by Imbalance Values[a]

0000–0300 UTC	% of Data	Imb	*Rn*	*H*	*LE*	*G*	u (m s^{-1})	*p* (kPa)	*T* (°C)
Imb < −25	18	−38	−52	15	−22	20	1.6	97.8	9.7
−25 ≤ Imb < −10	46	−18	−51	18	−8	23	1.4	98.0	11.9
−10 ≤ Imb <5	22	−3	−30	10	−6	23	1.0	97.9	9.6
Imb ≥ 5	14	27	−14	8	10	23	1.1	97.8	7.3

[a]Terms of the energy balance in W m^{-2}.

There is a linear variation of the imbalance with the net radiation, either during daytime or at night. A similar behavior is found for *H* and *LE* for values between 0 and −100 W m^{-2}, and for *G* between 0 and −60 W m^{-2}, all leveling off at larger values with imbalances between 100 and 150 W m^{-2}. Since these values of the fluxes typically correspond to daytime, we may state that the imbalance increases with the value of net radiation as well as with the sum of *H*, *LE*, and *G*.

At night, *H* and *G* are typically positive and *Rn* and *LE* are negative (except when there is condensation and *LE* is positive). The imbalance behaves linearly for *Rn* and for *LE* (either for positive and negative values), whereas *G* and *H* have essentially constant values, indicating a possible saturation of the response capacity of these fluxes to the vertical temperature gradients that are typically established at night in the air and soil.

3.4. Imbalance and the Meteorological Variables

In Figure 5, the main air and soil mean variables are represented against the imbalance, again averaging imbalance values inside each variable bin. In general, none of the variables show any clear relationship with the values of the imbalance, and the standard deviations are very large, indicating low statistical significance.

Nevertheless, there are a couple of issues worth noting. On one hand, warm and moist soils have very large imbalances, pointing to the effect of water conductivity and water phase changes as key processes in hot weather. On the other hand, the wind seems to indicate a two-modal distribution, with a local maximum

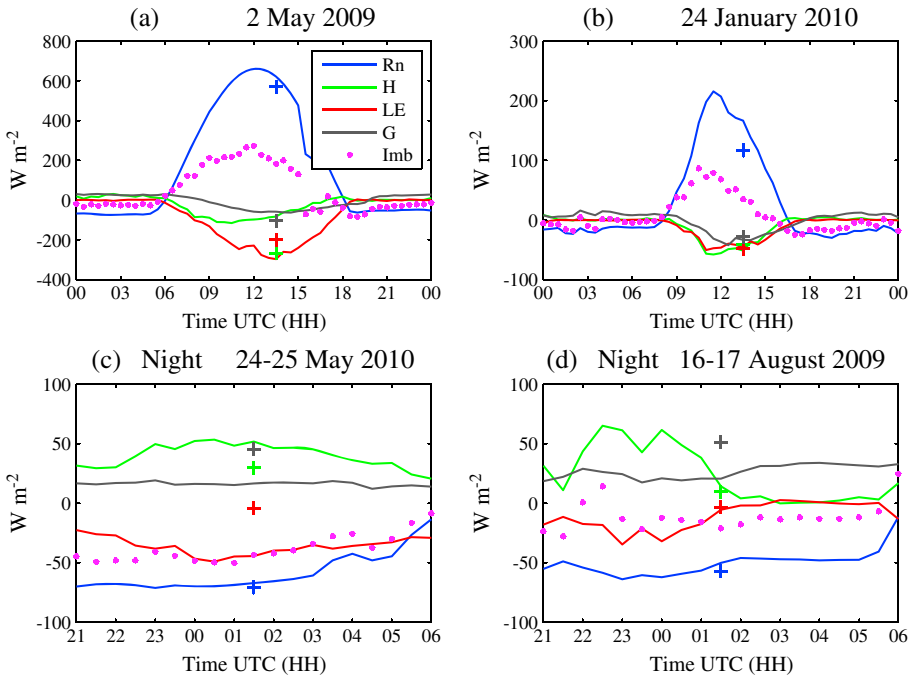

Figure 6. Terms of the surface energy budgets for selected days. (a) A clear day with weak winds, (b) a cloudy day with weak winds, (c) a night with a few scattered clouds and moderate wind, and (d) a clear night with very weak winds. The lines indicate the terms measured in the station, the violet symbols show the resulting imbalance and the crosses indicate the ECMWF model values at the center of the averaging intervals (1200–1500 UTC and 0000–0300 UTC). The symbols for the model have the same colors as the corresponding lines for the observations.

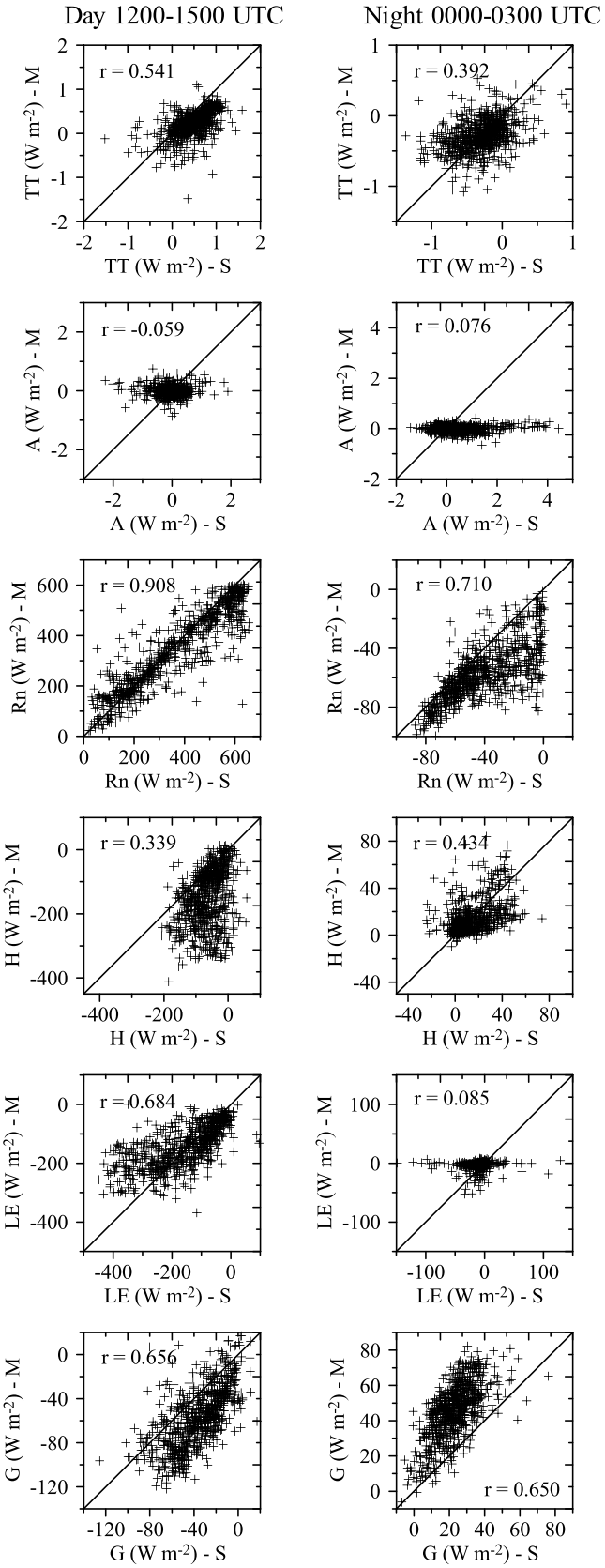

Figure 7. Observed versus ECMWF model values of the surface energy budget terms. (left) Averages for the interval between 1200 and 1500 UTC. (right) Averages for the interval between 0000 and 0300 UTC. (top to bottom) Tendency, advection, net radiation, sensible heat flux, latent heat flux, and ground flux. The 1:1 line is included for reference, as is the correlation coefficient.

of imbalance at approximately 1.5 m s^{-1}. Typically, the wind speeds found on fair weather days with dry or shallow cumulus convection are well correlated with high latent and sensible heat fluxes.

3.5. Imbalance and Weather

Tables 2 and 3 summarize the behavior of some of these quantities if we divide them into intervals, loosely based on the weather annotated by a human observer in the area. Values of 1200–1500 UTC show linear increases of the imbalance with almost all variables, except the already noted saturation of *H* and *G* for very large values of the imbalance. Analyses by day of the year (not shown) indicate that small imbalances (Imb < 60 W m^{-2}) are usually in winter with cloudy conditions, and sometimes rain, whereas moderate imbalances (60 ≤ Imb <100 W m^{-2}) are found mostly from fall to spring, on cloudy or windy days. Large imbalances (100 ≤ Imb < 150 W m^{-2}) are found between spring and fall, mostly on fair, cloudless days with weak wind. The largest values, which occur between May and September, correspond to days with very high evaporation values. Figures 6a and 6b show two examples of the SEB, one for a clear calm day with a great imbalance—in absolute value as large as the evaporation—(2 May 2009) and one for a cloudy day with weak winds (24 January 2010) where all the terms are smaller but the imbalance is proportionally as large as the previous one.

Nighttime shows less defined patterns (Table 3). The nights with very

high negative imbalances (Imb < -25 W m^{-2}) are of two types. On one hand, nights that are foggy, cloudy, or rainy are mainly concentrated in December and January. On the other hand, nights with relative high negative *LE* values, implying windy conditions and evenly distributed throughout the year. An example of a clear, windy night (25 May 2010) is given in Figure 6c, with both evaporation and net radiation being high and negative. This cooling is not compensated by the sum of *G* and *H*, and it may be used in water condensation in the soil or plants. The most frequent category ($-25 \leq$ Imb < -10 W m^{-2}) consists of calm, clear nights with dew and sometimes mist, equally distributed throughout the year. Figure 6d shows one of these nights (17 August 2009), when there is a certain constancy of *Rn* and *G* throughout the night, whereas the turbulent fluxes are significant in the first part of the night and practically die out after midnight, with the occurrence of some positive values of *LE* (condensation). For the other two intervals, there are usually clouds, rain or fog, with low-absolute values of *Rn*.

4. Comparison With ECMWF Values

4.1. The Surface Energy Budget in the ECMWF Model

Three-hour values of the terms of the SEB and other variables of interest were obtained from the ECMWF database for the nearest grid point to the Raimat station, and a comparison is made here to the values observed. We used the forecast starting at 0000 UTC to obtain the values for 1200–1500 UTC and one starting at 1200 UTC to obtain the 0000–0300 UTC values. The fundamentals of the soil vegetation model in the ECMWF model are described in *Viterbo and Beljaars* [1995]. In the soil, four levels are used and connected by a temperature diffusion equation, with the heat conductivity as a function of the volumetric water content as in *McCumber and Pielke* [1981]. The top boundary condition is the sum of *Rn*, *H*, and *LE*, whereas at the bottom (deeper than 3 m) zero heat flux is assumed. The upper boundary flux is expressed as proportional to the difference between skin temperature and the first ground temperature. The skin temperature (T_{sk}) intends to take into account the effect of vegetation and litter, it is assumed to have no heat capacity and therefore is the result of a SEB [*Viterbo and Beljaars*, 1995, equation (6)]:

$$(1-\alpha)R_s + \epsilon(R_t - \sigma T_{sk}^4) + H + LE + \Lambda(T_{G1} - T_{sk}) = 0 \tag{8}$$

where α, ϵ, and σ are, respectively, the albedo, the surface emissivity, and the Stefan-Boltzmann constant, R_s and R_t solar and terrestrial radiation are computed by the radiation scheme of the model, *G* is represented by the last term, T_{G1} is the temperature of the first ground level (−7 cm), and Λ is a parameter that plays the role of skin conductivity. *H* and *LE* are traditionally parameterized, using transfer coefficients dependent on thermal stratification and, in particular, on T_{sk}.

Therefore, for our purpose, $G = \Lambda(T_{G1} - T_{sk})$, $Rn_t = (1-\alpha)R_s + \epsilon(R_t - \sigma T_{sk}^4)$, *H* and *LE* will be compared to the measured values. However, *G* in the model is the residual of the other three terms because it is not stored in the ECMWF database.

4.2. Statistical Comparison to Data

4.2.1. Daytime

Table 1 provides the seasonal averages of the terms computed by the ECMWF compared to the observed ones. The model values of *TT* and *A* are of the same order of magnitude as the observed ones, with *A* systematically smaller for the model, most likely because the model heterogeneity of the 2 m temperature field is smaller than in reality (Figure 2). By inspecting the table simultaneously with the left column of Figure 3, which contains the evolution of the monthly averaged values, the model correctness can be assessed.

It is found for averages that *Rn* is well simulated, with differences below 10%, which are within the observational uncertainties [*Kohsiek et al.*, 2007]. *H* is severely overestimated by the model, especially in spring and summer, whereas *LE* is underestimated, indicating that the availability of soil water in reality is very different to what the model represents, most likely related to the treatment of irrigation, not explicitly included in the model. The differences between the model and observations for *H* and *LE* are minimal in winter. *G* is systematically larger in the model and is approximately double the average observations in fall and winter. These large values of *G* in the model could originate from an inadequate representation of the soil thermal characteristics, an incorrect temperature profile, and most likely because this term incorporates the entire imbalance.

If we inspect the individual averages shown in Figure 7 (left column), the maximum absolute model values of *LE* are approximately 300 W m^{-2}, while the observations can be greater than 400 W m^{-2}, making the

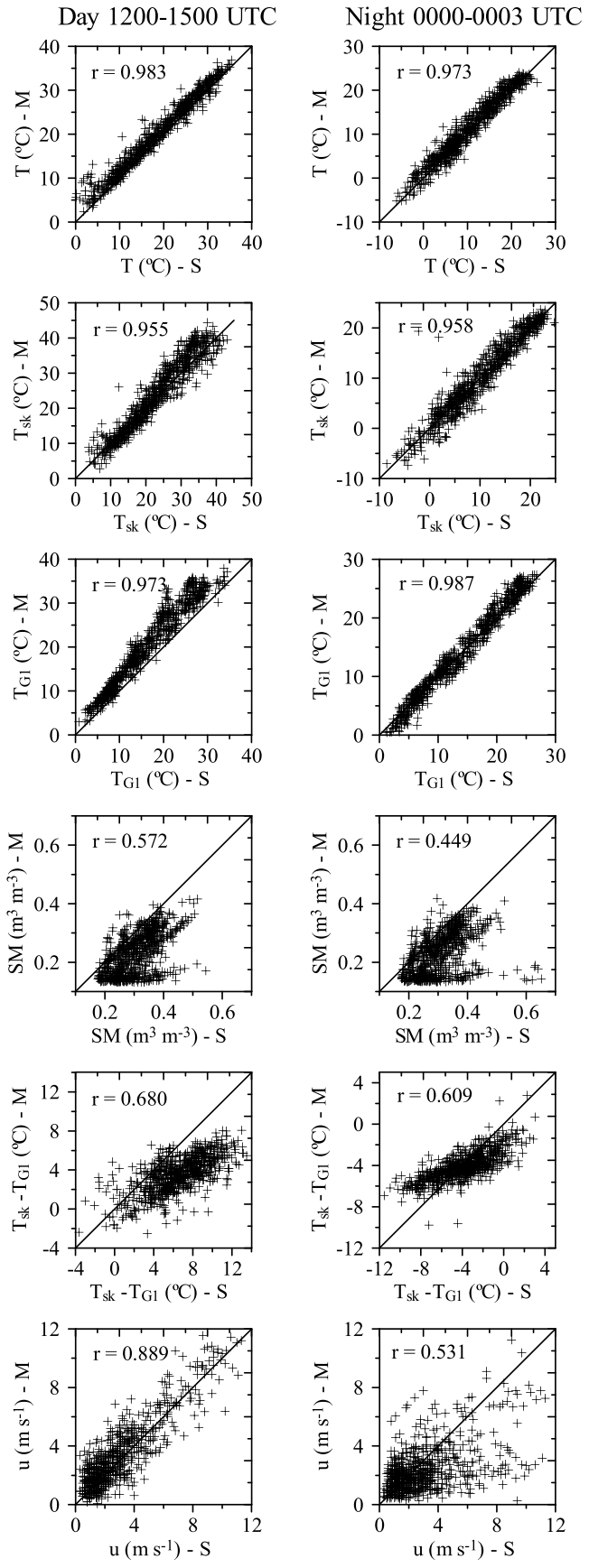

discrepancies evident for absolute values above 200 W m^{-2}. For *H* complementary behavior is observed, because the observations rarely exceed 200 W m^{-2}, while the model can reach more than 300 W m^{-2}. In general, *G* is larger in the model as previously indicated.

To provide more information about these discrepancies, Figure 8 (left column) compares key variables for the SEB equation terms. It is interesting to see that the model values for air and skin temperature are consistent with the observations. This means that the model successfully formulates the correspondence between these two magnitudes. The main differences are in the ground temperature and the soil moisture, where the first model level values are compared to the data taken at approximately 6 cm under the surface. Errors in ground temperature can easily be above 5°C, and soil moisture (SM, expressed as the volume of water over total volume) can be underestimated by nearly 50%, although observed SM values above 0.5 may correspond to water pooling on the surface. If th e difference ($T_{sk} - T_{G1}$) is compared, one can see that for values of more than 4°C, the observation may reach values that are greater than 12°C, whereas the model never exceeds 8°C. T_{sk} and *T* are well simulated by the model, implying that most of the differences lie in the soil component. Since *H*, *LE*, and *Rn* are well estimated, *G*, in fact, has to also address with the imbalance and, therefore, is overestimated, despite the soil in the model being warmer and drier, which should lead to smaller ground fluxes. The parameter Λ is a factor that may be adjusted if needed.

Figure 8 also shows that the modeled wind speed is consistent with

Figure 8. As in Figure 7, (top to bottom) air, skin and ground temperatures, soil moisture, difference between skin and ground temperatures, and wind speed.

Table 4. Values for the Four Selected Days of Figure 6 (Terms of the Energy Balance in W m^{-2})[a]

Day[b]	*Rn*	*H*	*LE*	*G*	Imb	SM(%)	T_{sk} (°C)	T_{G1} (°C)
02/05/2009, 1200–1500	587/571	−71/−268	−271/−199	−60/−103	185/0	26/23	25/28	17/22
24/01/2010, 1200–1500	143/117	−41/−41	−40/−48	−32/−28	30/0	34/31	14/12	9/10
25/05/2010, 0000–0300	−66/−71	48/30	−42/−4	16/45	−43/0	36/16	15/15	18/19
17/08/2009, 0000–0300	−51/−57	18/9	−8/−3	25/51	−16/0	27/15	20/22	24/26

[a]Left value: observation, right value: model.
[b]Dates are formatted as day/month/year.

observations implying that the model overestimation of *H* is most likely not produced by too large of a mechanical production of turbulence, but from a displaced value of the Bowen ratio. As an illustration, the values for the selected individual cases shown in Figure 6 are given in Table 4. The observed large midday summer imbalance of 2 May 2009 is closed in the model using much larger values of *H* and lower values of *LE*. The errors in the ground part (3°C for T_{sk}, 5°C for T_{G1}, 3% for SM) indicate that the model heats the soil more than the observations suggest, allowing more sensible heat flux to reach the surface, which is also warmer in the model, indicating that the heat missing in the observations (the imbalance) usually goes to *G* and *H* in the model.

The small daytime imbalance for a cloudy and windy day (24 January 2010) has quite a good correspondence between observed and model values of the budget terms and of the soil moisture and temperatures (Figure 6b and Table 4).

4.2.2. Nighttime

The 0000–0300 UTC values in Table 1 and the evolution of the monthly means (Figure 3, right column) show a main difference with respect to the daytime: the model systematically overestimates *Rn*. This is essentially counterbalanced by *G*, also overestimated by a factor between 1.2 and 2.8 depending on the month. *H* and *LE* have quantitatively far fewer differences with the data, although *LE* is almost always underestimated. Individual averages confirm this in Figure 7 (right column). For the other terms, it is interesting to note that *H* in the model has very few negative values in Figure 7, contrary to the significant occurrences in the observations, and that the number of condensation events (positive *LE*) is also less in the model than observed.

Looking at the key variables for the surface processes (Figure 8, right column), air, surface, and also ground temperature are consistent to observations. The SM is underestimated as it was during daytime, most likely because this variable changes very slowly in the model. The wind forecast is worse than during the daytime, but since *H* is not the key factor, this is not relevant. The difference ($T_{sk} - T_{G1}$) is always negative in the model (surface colder than the ground), but no major differences between the model and the observations appear.

Inspecting the two nighttime cases of Figures 6c and 6d (values in Table 4), we see that for the windy night with scattered clouds (25 May 2010) the main difference lies in *LE*, which is underestimated in the model that has a SM value much lower than the observations. A clear night with calm winds has, in 3 h average, a very small contribution to water phase changes for either the observations or the model, and the main difference lies in *G*, which is higher in the model despite the lower SM contents compared to the observations.

5. Conclusions

The imbalance in the determination of the SEB is an issue that deserves continuous exploration. Here a formal derivation of the processes hidden in this term has been made using the prognostic temperature equation for a conceptual volume. This formalism allows measurements not located at the same level to be treated together. The imbalance contains the temperature tendency, the advections due to the surrounding heterogeneities, the storage of heat in the volume, the exchanges of heat with the air due to biological processes, unmeasured water phase changes in the soil and surfaces, and any instrumental indetermination, in addition to other processes that may have been neglected.

The inspection of the observed SEB for a location in the eastern Ebro Valley (Catalonia, Spain) has shown that local tendencies and horizontal advection of temperature for scales larger than a few kilometers contribute very little to the imbalance. The same hypothesis is made for the storage and the biological processes for the test site, where the mass of the elements in the volume is small. It can be considered that the main driving term is the net radiation, which shows a well-defined annual cycle during the daytime but no clear cycle at night.

The diurnal radiation heating is mostly compensated by *LE* and *H*, the former usually larger than the latter because of the large availability of water due to irrigation. *G* is of the order of 10% *Rn*, whereas the resulting imbalance is approximately 30%. The nocturnal radiation cooling is essentially counteracted by *G*, while *H* and *LE* are significantly smaller. *LE* at night is often positive indicating condensation and warming.

The imbalance shows a well-defined linear relation with *Rn*. The largest imbalances take place on warm days, when the values level off despite increasing values of *H*, *LE*, and *G*. Analyses of the frequencies and of particular cases indicate that very large imbalances are related to high values of soil moisture, especially in warm conditions.

Data are compared to the corresponding computations for the same point made by the ECMWF model separately for two 3 h time intervals for noon and midnight. In the daytime, there is a significant difference in the Bowen ratio, because the model is drier than the observations for this point. Despite this, *G* is larger in the model, where lower soil moisture causes less ground heat flux. This may come from the fact that *G* is, in practice, the residual of the other three terms (*Rn*, *H*, and *LE*) and may be overestimated. The good representation of the variables by the model indicates that the differences are taken into account by adapting parameters of the model such as the skin or ground thermal conductivities.

In the comparison for the nighttime, *Rn* and *G* essentially counteract each other, but their values are higher in the model than in the observations. The model values of air, surface, and skin temperature are well simulated, but the soil moisture is again typically underestimated by a factor of 2. The high-model values of *Rn* and *G* on clear, calm nights are most likely related to the emissivity and thermal conductivity changes due to the soil moisture, whereas the windy nights observed imbalances may be related to the insufficient amount of evaporation from the ground.

The results of this study show that, for a site of moderate terrain heterogeneity, the imbalances are similar to the ones found for other studies, therefore allowing the technique to be used for nonhomogeneous sites if the imbalances are documented. The imbalance behaves similarly to the other terms of the SEB equation, approximately 30% of the value of *Rn* on average, although for individual cases the amount can vary significantly below or above this value. Which components contribute most to the imbalance still need to be determined, and this is most likely function of the type of terrain and its uses. Models impose the closure of the SEB equation; therefore, if one term is computed as the residual, it will include all of the uncertainties, causing an error that will have to be corrected by means of tunable parameters in their physical schemes.

Acknowledgments

This work was partially supported by grant CGL2012-37416-C04-01 of the Spanish Ministry of Economy and Competitiveness, supplemented with FEDER funds, and by a JAE-DOC contract of the Spanish National Research Council (CSIC). We would like to thank the ECMWF User Support Team for its very generous and dedicated help in obtaining the data, via the "Atmospheric Boundary Layer in Complex Terrain" Special Project. The Meteorological Service of Catalonia kindly provided the data for the analysis. Armand Alvarez took notes on the weather on a daily basis, and Felipe Molinos organized the database.

References

Bastiaanssen, W. G. M., M. Menenti, R. A. Feddes, and A. A. M. Holtslag (1998), A remote sensing surface energy balance algorithm for land (SEBAL). 1. Formulation, *J. Hydrol.*, *212*, 198–212.

Cuxart, J., and M. A. Jiménez (2012), Deep radiation fog in a wide closed valley: Study by numerical modeling and remote sensing, *Pure Appl. Geophys.*, *169*(5–6), 911–926.

Cuxart, J., J. Cunillera, M. A. Jiménez, D. Martínez, F. Molinos, and J. L. Palau (2012), Study of mesobeta basin flows by remote sensing, *Boundary Layer Meteorol.*, *143*(1), 143–158.

Foken, T. (2008), The energy balance closure problem: An overview, *Ecol. Appl.*, *18*(6), 1351–1367.

Foken, T., M. Mauder, C. Liebethal, F. Wimmer, F. Beyrich, J.-P. Leps, S. Raasch, H. A. R. DeBruin, W. M. L. Meijninger, and J. Bange (2010), Energy balance closure for the LITFASS-2003 experiment, *Theor. Appl. Climatol.*, *101*(1–2), 149–160.

Garratt, J. R. (1992), *The Atmospheric Boundary Layer*, 319 pp., Cambridge Univ. Press, Cambridge, U. K.

Kohsiek, W., C. Liebethal, T. Foken, R. Vogt, S. P. Oncley, C. Bernhofer, and H. A. R. De Bruin (2007), The Energy Balance Experiment EBEX-2000. Part III: Behaviour and quality of the radiation measurements, *Boundary Layer Meteorol.*, *123*(1), 55–75.

Leuning, R., E. Van Gorsel, W. J. Massman, and P. R. Isaac (2012), Reflections on the surface energy imbalance problem, *Agric. Forest Meteorol.*, *156*, 65–74.

Mauder, M., S. P. Oncley, R. Vogt, T. Weidinger, L. Ribeiro, C. Bernhofer, T. Foken, W. Kohsiek, H. A. R. De Bruin, and H. Liu (2007), The Energy Balance Experiment EBEX-2000. Part II: Intercomparison of eddy-covariance sensors and post-field data processing methods, *Boundary Layer Meteorol.*, *123*(1), 29–54.

McCumber, M. C., and R. A. Pielke (1981), Simulation of the effects of surface fluxes of heat and moisture in a mesoscale numerical model: 1. Soil layer, *J. Geophys. Res.*, *86*(C10), 9929–9938.

Martínez, D., J. Cuxart, and J. Cunillera (2008), Conditioned climatology for stably stratified nights in the Lleida area, *Tethys J. Weather Clim. Western Mediterranean*, *5*, 13–24.

Moderow, D., M. Aubinet, C. Feigenwinter, O. Kolle, A. Lindroth, M. Mölder, L. Monyagnani, C. Rebmann, and C. Bernhofer (2009), Available energy and energy balance closure at four coniferous forest sites across Europe, *Theor. Appl. Climatol.*, *98*(3–4), 397–412.

Oke, T. (1987), *Boundary Layer Climates*, vol. 5, 435 pp., Routledge of Taylor & Francis.

Oncley, S. P., et al. (2007), The Energy Balance Experiment EBEX-2000. Part I: Overview and energy balance, *Boundary Layer Meteorol.*, *123*(1), 1–28.

Sánchez, J. M., W. P. Kustas, V. Caselles, and M. C. Anderson (2008), Modelling surface energy fluxes over maize using a two-source patch model and radiometric soil and canopy temperature observations, *Remote Sens. Environ.*, *112*(3), 1130–1143.

Viterbo, P., and A. C. M. Beljaars (1995), An improved land surface parameterization scheme in the ECMWF model and its validation, *J. Clim.*, *8*(11), 2716–2748.

Viterbo, P., A. C. M. Beljaars, J. F. Mahfouf, and J. Teixeira (1999), The representation of soil moisture freezing and its impact on the stable boundary layer, *Q. J. R. Meteorol. Soc.*, *125*(559), 2401–2426.

Webb, E. K., G. I Pearman, and R. Leuning (1980), Correction of flux measurements for density effects due to heat and water vapour transfer, *Q. J. R. Meteorol. Soc.*, *106*(447), 85–100.

Yue, P., Y. Li, Q. Zhang, and L. Zhang (2012), Surface energy-balance closure in a gully region of the Loess Plateau at SACOL on eastern edge of Tibetan Plateau, *J. Meteorol. Soc. Jpn.*, *90C*, 173–184.